Enhancing the barrier effect of sol-gel derived inorganic coating by doping h-BN nanosheet

Yu Shi, Sheng Yuan, Benoît Ter-Ovanessian, Ying Huo, Bernard Normand

Enhancing the barrier effect of sol-gel derived inorganic coating by doping h-BN nanosheet

Yu Shi[1], Sheng Yuan[1,*], Benoit Ter-Ovanessian[1], Kurt Hermange[1], Ying Huo[1,2], Bernard Normand[1]

[1] Universite de Lyon, INSA-LYON, MATEIS UMR CNRS 5510, 69621 Villeurbanne Cedex, France

[2] Ecole Centrale de Lyon, INSA-LYON, LTDS UMR CNRS 5513, F-69134 Ecully cedex France

[*] Corresponding author: tel +33 4 72 43 71 44 ; E-mail address: sheng.yuan@insa-lyon.fr

Fill address: Bat. L. De Vinci, 21, Rue de Jean-Capelle, 69100, Villeurbanne, France

Abstract

Nanocomposites filled with impermeable two-dimensional materials are of specific interest for protecting metal from corrosion. The addition of hexagonal boron nitride nanosheet (BNNS) into a coating matrix can improve the barrier effect virtually due to its high chemical and thermal stability and dielectric property. This atom-level thick filler involves a « tortured pathway» that prolongs the penetration distance to the substrate. In this study, BNNS was added into a zirconium coating prepared via sol-gel way. In order to understand the influence of nanosheets size on the barrier performance, three h-BN grades were used. It was intended to keep all the other elaboration parameters constant so that the electrochemical behavior variation is mainly attributed to the nanosheet size. The morphology and microstructure of hexagonal boron nitride flakes in different exfoliation level and the nanocomposite coating were studied by SEM, HRTEM, SAED, FTIR cartography, Raman spectroscopy. Meanwhile, the corrosion resistance of composite coatings was characterized by polarization test and long-term electrochemical impedance spectroscopy in a 3.5 wt% NaCl solution.

Keywords: h-BN nanosheet; 2d material; sol-gel; nanocomposite coating; barrier effect

1. Introduction

Growing with the continuous progress on graphene, two-dimensional (2D) materials such as hexagonal boron nitride (h-BN), MoS_2, clay have attracted extensive attention owing to the unique layered structure in atomic scale.[1,2,3,4] Recent researches show the raising interests related to the 2D materials for metal protection against oxidation and corrosion.[5,6,7] It has been proved that graphene is almost impermeable to most small molecules, including oxygen, water molecule, and even the molecule as small as helium.[8] However, graphene is well-known for its outstanding electrical conductivity that can potentially lead to even worse resistance for oxidation than the bare metal.[9] By this token, h-BN nanosheet (BNNS), having a similar molecule impermeability,[10] is a better choice as a protective barrier thanks to its excellent thermal and chemical stability and electrical insulation.[11,12]

BNNS can be applied in two different ways. In the first one, BNNS is directly deposited on a metal surface by CVD or CVD-derivatives methods or transferred from another carrier.[13,14] The presence of this atom-level thick layer modifies the surface energy and provides a water-repellency to prevent the direct contact of water and oxygen molecules to the underlying metal.[15] The application of this methodology suffers from the significant drawback associated with the difficult control on defects level, on the number of layers, and on the pollution during the transfer process.[16,17]

On the other hand, BNNS has also been incorporated into various matrix to obtain high-performance nanocomposite coating. The self-standing BNNS is usually elaborated by the liquid-phase exfoliation (LPE) method to split h-BN atomic layers from bulk flake and to disperse them in a suitable solvent.[18,19] Many elsewhere researches have reported the validity of adding these BNNS in organic or hybrid coatings. For instance, in resin20, polyimide,[21] PVA[22], and PMMA[23] matrix, the nanocomposite coatings showed reinforcement on barrier property against corrosion in different cases. A relatively high concentration of the nanofiller is usually required to maximize the nanocomposite barrier effect. Cui et *al.* have studied the influence of BNNS content in water-borne epoxy coating, in which the best anti-corrosion performance was obtained with 1*wt%* of BNNS.[24] However, the aggregation drastically limits the pristine BNNS concentration in different solvents due to the strong "lip-lip" interaction between neighboring layers.[25] The development of chemically modified BNNS or other additives assisting methods can resolve this problem to a certain extent.[26,27] As reported elsewhere, the BNNS modified by 3-glycidoxypropyltrimethoxisilane (GPTMS) or underwent a plasma treatment have been proved a better dispersibility in acrylic coating for steel protection.[28,29]

From a new perspective, replacing the commonly used organic matrix by an inorganic one reduces the BNNS content for the reinforcement significantly. Especially, the high crosslinking in a Sol-Gel matrix and the shrinkage during the drying process strengthen the barrier effect of the nanocomposite significantly.

In this work, we prepared zirconium oxide coating enhanced by BNNS fillers via sol-gel on 316L stainless steel and investigated the electrochemical properties of this coating system. The zirconium matrix was chosen due to the ease to elaborate, the electrical insulation, the low mismatch of thermomechanical stress at the steel/coating interface, and the chemical inertness. It is worth mentioning that the durability of the inorganic coating essentially relies on two parts: the coating itself and the coating/ substrate interface. In order to avoid the interface breakdown, the resistive 316L was applied to provide a good adhesion with the coating and a relatively low reactivity under corrosive conditions. Removing the interface factor, we highlighted the influence of BNNS size on the barrier effect of such a nanocomposite coating.

2. Materials and procedure

2.1 Materials

Stainless steel 316L (C 0.03%, Cr 18.00%, Ni 10.00%, Mo 3.00%, Mg 2.00%, Si 0.75%, P 0.045%, S 0.03%, N 0.10%, balanced by iron, GoodFellow) were cut into 50 x 25 x 3 mm^2 samples and grounded up to 1200-mesh SiC. Zirconium (IV) acetate hydroxyl (ZAH) was used as the precursor (*Sigma Aldrich*) for sol-gel coating. Three h-BN powders, named BN-A, BN-B, and BN-C, were used (*GoodFellow*) with different average flake sizes to prepare BNNS

2.2 Preparation of BNNS colloidal solution

The raw of BN powders were added in distilled water with a concentration of 3 mg/mL. The mixtures were treated in an ultrasonic bath (ELMA P30H) for 12h. The BNNS suspension was centrifuged for 90min at 1500 rpm to obtain a "milk-like" solution. The newly prepared BNNS solution could stay stable from aggregation for one week.

2.3 Preparation of substrate, zirconium oxide Sol and coatings

316L substrates were rinsed in distilled water and ethanol using an ultrasonic bath for 15min. In order to improve the adhesion, 316L substrates were immersed in a "piranha" solution (H_2O_2: H_2SO_4 = 1 : 2) for 15 minutes. The piranha solution is commonly used for removing all contaminants from the metal surface and for forming a recovery hydroxyl layer on the surface, which provides strong adhesion with the Sol-Gel coating.[30]

Zirconium oxide Sol was prepared by dissolving 3 mg of ZAH precursor in 50 ml absolute ethanol and 2.5ml of acetone. The pH of the colloidal solution was buffered by acetate acid at 3.2, which allows a relatively good stability for the colloidal solution.[31] The BNNS colloidal solutions were slowly injected to sol-gel solution keeping the water : Zr molar ratio superior to 4. As a reference, a Sol with equivalent distilled water was prepared for pure zirconium oxide coating without BNNS.

All coatings were deposited by three dipping process and underwent a heat treatment at 120 °C for 24 hours to obtain a xerogel film. The sample coated with different BNNS are named ZrO/BN-A, ZrO/BN-B, ZrO/BN-C, respectively. The coating without filler is named ZrO.

2.4 Characterization

The concentration of BNNS was estimated using UV-visible spectra (UVline 9400) in a quartz cuvette Beer-Lambert's law:

$C/l=\alpha A$ equation 1)

Where the concentration of the charge, C, is linearly proportional to the absorption intensity A, l is the interaction path length and α represents the extinction coefficient.

Scanning electronic microscopy (SEM) was performed with a ZEISS Supra55. High-Resolution Transmission Electron Micrographs (HRTEM) and the Selective Area Electron Diffraction (SAED) were performed on the JEOL-2010 microscope operating at 200 kV. Infrared microspectroscopy (IR) was recorded in ATR mode on the coated systems ThermoScientific Nicolet iN10. The Raman scattering measurement was performed on Horiba Aramis using wavelength 514nm. The Dynamic Light Scattering Spectroscopy (DLS) and zetapotential measurement was applied using the Zetasizer (Malvern, nano ZSP) from INSA de Lyon, France.

2.5 Electrochemical measurement

The polarization curve was acquired for a scanning range from -50 mV *vs.* OCP to 1000 mV *vs.* SCE with a scanning rate of 0.167mV/min. The Electrochemical Impedance Spectroscopy (EIS) of different samples were recorded after different immersion time in 30 g/L NaCl solution. EIS tests were carried

out with a frequency varying from 100 kHz to 3 mHz, the amplitude of the scanning potential was fixed at 15mV *vs.* OCP.

Electrochemical impedance spectroscopy (EIS) measurements were performed on a Biologic SP300 potentiostat in a three-electrode cell, including a carbon counter electrode, a saturated calomel electrode (*SCE*) as the reference electrode, and the coated samples as the working electrode. The impedance of a constant phase element (CPE) can be calculated using the equation:[32]

$$Z_{CPE} = \frac{1}{Q(j\omega)^{\alpha}} \qquad \text{equation 2)}$$

α is the exponent of CPE, the *j* is the imaginary number, ω is the angular velocity.

3. Result and discussion

3.1 Characterization of Sol and BNNS suspension

BNNS was exfoliated from the three raw h-BN powders in aqueous media. Fig. 1 shows the morphology and the size distribution of these pristine powders, which gives the statistic average flake sizes of 7, 4.5, and 0.95 µm for BN-A, BN-B, and BN-C, respectively (see Fig. 1 inset). Although the nanosheet may have a reduction of the basal plan dimension compared with the raw materials after ultrasonic treatment,[33,34] we expect that the so-prepared BNNS sizes keep consistent sequence with the BN flakes under such a mild exfoliation conditions.

The state of BN flakes was probed by HRTEM during the exfoliation. Fig. 2a shows the TEM images corresponding to the slim down BN flakes. The selective area electron diffraction (SAED) pattern exhibits hexagonal bright dots (inset), which are representative for single h-BN crystals. The Moire patterns in Fig. 2b indicates misorientation between h-BN layers induced by the exfoliation process around the *c-axis*. In the final colloidal solution, the BNNS has a two-dimensional structure with a thickness of a few atomic layers approaching to that of the graphene, as shown in Fig. 2c.

The concentration of BNNS in the colloidal solution can be evaluated by UV-Visible spectroscopy. We can observe the characteristic band of h-BN at a wavelength λ = 209 nm in the absorption spectra recorded with all three Sol, see Fig. 3. To avoid scattering influence, we chose to use the adsorption intensity at λ = 300 nm.[35] The corresponding extinction coefficient α in equation 1 has been determined by calibrating the UV-Visible spectroscopy to the weighting result, giving the α value of 2924 mg /ml/m. This value is in good agreement with the literature.[36] The concentrations of different BNNS were estimated of around 15 µg/mL for all three different BN derived solutions, which is close to the concentration reported elsewhere using a similar preparation way in water.[37]

The colloid size matters mostly the sol-gel coating's physicochemical properties and microstructure. Fig. 4 shows the evolution of colloid size in Sol during three days after mixing with the BNNS solution. The colloid size distribution remained almost unchanged and displayed two peaked colloidal size around 7 and 50 nm, respectively. It has been complied furtherly with the same aging time of Sol to prepare all coatings and vigorously stirred each nanocomposite Sol before deposition in order to limit the agglomeration. It's essential to notice that each nanocomposite sol has very closed colloids size distributions and concentrations to each other. Therefore, the changes in nanocomposites sol-gel coating's electrochemical behaviors are mainly induced by the different BNNS size.

3.2 Characterization of the coating

The coatings were transparent, homogeneous, and recovering without any remarkable defect on the top surface. Fig. 5 shows one typical top view on ZrO/BN coating since the presence of the different BNNS affects the coating's morphology barely. The fractography of the coating reveals a thickness of 300 - 400 nm prepared by three dippings. It is interesting to notice that one layer thickness is one-tenth of the nanosheet surface dimension, while it is 100 times bigger than the nanosheet thickness. In this

way, we can tune the orientation of the nanosheets in the matrix, as shown in Fig. 5d. The nanosheets were smeared and oriented by the capillary force on the tip of Sol deposited on the substrate. Fig. 5e and f show that the 2D materials stay in parallel with the dipping direction within the coatings.

The pure zirconium oxide coating is hydrophilic, showing a water contact angle of 65°. Doping BNNS into coating, the contact angle becomes 102°, meaning the coating transforming to a hydrophobic surface.[38] It seems the hydrophobic BNNS covers part of the polar groups on the coating surface. This finding is interesting as the hydrophobic surface can reduce the interaction with polar electrolyte and increase the coating anti-corrosion performance. Moreover, the raw BN flakes size impacts the water contact angle barely.[39]

From the Fourier Transform Infrared spectroscopy (FTIR) shown in Fig. 6, the bands at a wavenumber of 1570 cm^{-1} and 1440 cm^{-1} characterize the acetate anti-symmetrical and symmetrical stretching vibration of -CO_2 groups issued from the sol-gel matrix, respectively.[40,41] The peak at 1350 cm^{-1} is related to B-N stretching (indicated by arrow), which can be observed in the spectra obtained with all three ZrO/BN, while it lacks in the pure ZrO sample.[42] The peak presented at 1025 – 1058 cm^{-1} corresponds to C-O stretching due to the existance of acetate groups.[43] The intensity observed at 700 cm^{-1} and 530 cm^{-1} are related to the Zr-O-Zr of the matrix which are common for all samples.[44,45] The intensity mapping of this band is reasonably homogenous within a surface area of 60 µm x 60 µm, indicating a good dispersion of the BN nanosheet. The barrier effect of the coating is closely linked with the homogeneity of the BNNS distribution. The area with low-density BNNS in the coating can weaken the barrier effect of the entire coating.

Besides, the BNNS distribution was confirmed with Raman spectroscopy on randomly selected ten points from the coating surface. Because of the similarity, Fig. 7 shows only three of them. The peak marked at a Raman shift of 1386 cm^{-1} is attributed to the E_{2g} mode vibration of B-N bonding.[46] The bands around the Raman shift of 600-650 cm^{-1}, 920 $cm^{-1,}$ and 970 $cm^{-}1$ are attributed to the amorphous phase of zirconium oxide.[47,48]

3.3. Influence of the BNNS morphology on potentiodynamic polarization test

The polarization curves for the bare and coated substrate are plotted in Fig. 8. The curves related to 316L exhibit a corrosion potential of 37mV/SCE. The low current density between 37 mV/SCE to 560 mV/SCE confirms the passive state of the sample. [49,50] The current transient informed about metastable pits.[51] When the potential exceeds 680 mV/SCE, the current density increases drastically, characterizing pitting propagation.

All coated samples showed higher E_{corr} than bare 316L substrate. The barrier effect provided by zirconium oxide, ZrO, coating is more effective than passive film since the current density is significantly lower than the one recorded with passive stainless steel. No current transient of metastable pit can be observed. Overall, under the sol-gel coating protection, the current density of the system shows a stage until a potential getting as high as 1100 mV/SCE.

For ZrO/BN-B, at the early stage of the anodic part, the current density is, however, higher than ZrO coating. This phenomenon can be explained by that the weaker barrier effect of ZrO coating will cause a higher oxidation rate on the metal surface. Thus, the accumulation of the oxidation product within pores of the coating lowers the current density. However, once the potential reaches the value where the metastable pitting corrosion happens, around 560 mV/SCE, the current density of ZrO surpass that of ZrO/BN-B. The pure sol-gel coating and ZrO/BN-C display similar behavior under polarization conditions. It seems that the smaller sized BNNS cannot influence the barrier properties. The oxidation rate on the metal surface is almost the same as in the case of ZrO.

The polarization curve of ZrO/BN-A shows a higher E_{corr} than ZrO/BN-B and ZrO/BN-C, as well as a lower current density, which is one order of magnitude lower at the beginning part of the anodic curve. The lower current densities are obtained from larger BNNS size, which seems to promote the

corrosion resistance of the coated system. It prolongs the pathway of the corrosive reactants and oxidation products significantly.

In brief, the BNNS filled coating shows improved barrier property, except for BN-C. We can define the critical nanofiller size d_c as the minimum size necessary to influence coating barrier property. It has:

1) When the BNNS average size, $d < d_c$, the nanofiller is too small to seal the pores within the coating, the electrochemical test mainly characterized sol-gel matrix properties while under deposit reaction plays a major role.
2) When $d \approx d_c$, the larger sized BNNS starts to seal the pores inside the coating and reduce the oxidation rate. Due to the similar size of BNNS and the pores, the penetration pathway is not largely prolonged. The mass transfer and oxidation reaction rates are nearly equivalent.
3) When $d > d_c$, the efficiently enhanced barrier effect leaves the pores sealed by the impermeable nanosheet. The mass transfer has to take the "zig-zag" way to reach the metal surface. At the same time, the system's resistance is predominated by the mass transfer process.

In general, the three different situations correspond to the cases of ZrO/BN-A, ZrO/BN-B, and ZrO/BN-C, respectively. It is important to note that the critical dimension d_c is not an absolute value but depends closely on the morphology of the sol-gel matrix. The interfacial behavior between the nanofiller and the matrix is also critical to ensure a good sealing effect. Indeed, the lack of adhesion allows the corrosive reactant to bypass the impermeable BNNS to the barrier property's detriment. Meanwhile, the doping quantity is another vital parameter that can influence the d_c value for a coating system. The prediction of this critical size is another interesting topic that will be discussed in a further study.

Fig. 9 shows the surface morphology after the polarization tests. The bare 316L is deeply corroded since the bulk dissolution of the metal can be observed. From the zoom image, it is observed that the pitting propagates into the coating. There are some oxidation sites on the coated surfaces, but no coating crack can be observed. Among all, ZrO/BN-A shows an almost untouched surface proving its excellent anti-corrosion performance.

3.4. Long term EIS

Hereafter, ZrO/BN-A coating was chosen for long-duration EIS analysis. The Nyquist and Bode plots of bare substrate, pure ZrO, and ZrO/BN-A sample are depicted in Fig. 10. The EIS results were recorded after 16 hours, 32 hours, 60 hours, and 120 hours immersion in NaCl solution. The decrease of the semicircle loop (black arrow) of 316L over time indicates that the barrier effect of passive film decreases during OCP. Meanwhile, unlike the case of 316L, the Nyquist curves of ZrO showed a similar diameter of the impedance circuit compared with 316L for 16 hours of immersion. This diameter reduces from 16h to 120h and remains stable. In contrast, the ZrO/BN-A shows a significantly enhanced resistance during the whole immersion time. By this token, the values obtained from the fitting of the impedance diagram are discussed from the duration of immersion extended to fifty days (1200h) (red arrows).

The EIS results are fitted by the numerical tool using an electrochemical equivalent circuit (EEC) model with two time constant depicted in Fig. 11a for 316L and Fig.11b for ZrO and ZrO/BN-A. The EEC for 316L, as shown in Fig. 11a, is different than the one which is classically used for passive film. Boissy et al. have proposed multiple models for the fitting of 316L in different cases.[52] Generally, the EEC describes a barrier effect that is controlled by the semiconductive properties of the passive film. In the case of this study, we consider that the chloride ions have contaminated the passive film and weakened the passive film. The passive film exhibited a structure with the oxide and hydroxide

sub-layer that could be simulated by a resistance behavior and Constant Phase Element (CPE) for a capacitance (R_{film}/Q_{film}). [53] The defects induced by the Cl^- stimulates the reactivity of stainless steel and can be characterized by a material exposure, which can be simulated by a charge transfer resistance and CPE for the double layer capacitance (R_{ct}/Q_{dl}).

For ZrO, the zirconium oxide shows inertness, leading to a quite similar phenomenon in the signal of EIS comparing to 316L. The EEC for ZrO is thus the same as the EEC of 316L. As shown in Fig. 11b, the only difference between the EEC for ZrO than for 316L is the R_{coat}/Q_{coat} replacing the R_{film}/Q_{film} to describe the behavior of the inert coating enhanced passive film, where the R_{coat} characterz the resistance in the coating pores.[54] Similarly, as the BNNS shows inertness and stability, the EEC of ZrO/BN-A is the same as the one of ZrO.

In this study, the numeric fittings have been carried out with respect to the α and Q value calculated graphically from the original data. Indeed, by plotting the imaginary part as a function of frequency in the logarithm scale, the slope of this curve directly gives α value.[55] The fitting curves are shown in Fig. 10 as well with solid lines. The associated fitting parameters of EIS recorded after 16h and 120h of immersion are listed in Table 1. Especially, there is a third parameter column for ZrO/BN-A after 1200h of immersion.

By comparing them, all the parameters of bare 316L kept almost constant after 16h and 120h of immersion, except for R_{film}, R_{coat} and R_{ct}. The evolution of R_{film}, R_{coat} and R_{ct} of all samples over 120h are shown in Fig. 12. It can be seen that the overall resistance ($R_{film} + R_{ct}$) of 316L decreased due to interaction with surrounding chloride ions. Meanwhile, for pure ZrO coating, we can not observe such a trend. As mentioned in the polarization section, the oxidation reaction and the ions exchange through the sol-gel film stay in an equilibrium state. Therefore, the localized corrosion and the repassivation of the metal surface establish a delicate equilibrium state.

In the case of ZrO/BN-A, it displays higher overall resistance ($R_{coat} + R_{ct}$) after 16h of immersion than the pure inorganic coating, which is benefited from the impermeable BNNS. This enhancement is classically explained by the "tortured pathway" mechanism that involves a prolonged diffusion length in the coating for the corrosive species to penetrate through the dense charge. This low mass transfer velocity causes an accumulation of oxidation products in the mesopores, which rises further the resistance of the coating. Moreover, different from the stable α_{coat}, the CPE exponent α_{dl} of Q_{dl} concurrently increase from 0.52 to 0.85, as shown in Fig. 13. This evolution reveals a transition of the diffusion process to a pseudo-capacitive behavior, implying more and more difficult for the exchange of ions on the metal surface.

4. Conclusion

Zirconium oxide coating doped with BNNS have been successfully synthesized via the sol-gel method on 316L. We prepared the nanocomposite coatings with the BNNS issued from three different raw BN powders that have different average grain sizes. When BNNS size is inferior to the critical size d_c, the electrochemical reactivity is predominated by the oxidation reaction at the initial stage of the anodic curve. When the BNNS size is superior to d_c, the coating shows an excellent barrier effect where the material exchange is significantly slow down. Long-term EIS were recorded with the nanocomposite coating after fifty days of immersion. The fitting results display an enhanced corrosion resistance due to the tortured diffusion path compared with pure sol-gel coating. Moreover, the double layer on the bottom of the pores became more and more homogenous and displayed an enhanced capacitive behavior, which is proved by the increase of α_{dl}.

Acknowledgements

I'm greatful for China Scholarship Council (Beijing, China) to fund this thesis.

Reference

[1] Balandin, A. A.; Ghosh, S.; Bao, W.; Calizo, I.; Teweldebrhan, D.; Miao, F.; Lau, C. N. Superior Thermal Conductivity of Single-Layer Graphene. Nano Lett. 2008, 8 (3), 902–907. https://doi.org/10.1021/nl0731872.

[2] Dikin, D. A.; Stankovich, S.; Zimney, E. J.; Piner, R. D.; Dommett, G. H. B.; Evmenenko, G.; Nguyen, S. T.; Ruoff, R. S. Preparation and Characterization of Graphene Oxide Paper. Nature 2007, 448 (7152), 457–460. https://doi.org/10.1038/nature06016.

[3] Rozhkov, A. V.; Sboychakov, A. O.; Rakhmanov, A. L.; Nori, F. Electronic Properties of Graphene-Based Bilayer Systems. Physics Reports 2016, 648, 1–104. https://doi.org/10.1016/j.physrep.2016.07.003.

[4] Georgakilas, V.; Tiwari, J. N.; Kemp, K. C.; Zboril, R. Noncovalent Functionalization of Graphene and Graphene Oxide for Energy Materials, Biosensing, Catalytic, and Biomedical Applications. Chem. Rev. 2016, 116 (9), 5464–5519. https://doi.org/10.1021/acs.chemrev.5b00620.

[5] Chen, S.; Brown, L.; Levendorf, M.; Cai, W.; Ju, S.-Y.; Velamakanni, A.; Piner, R. D.; Kang, J.; Park, J.; Ruoff, R. S. Oxidation Resistance of Graphene-Coated Cu and Cu/Ni Alloy. ACS Nano 2011, 5 (2), 1321–1327. https://doi.org/10.1021/nn103028d.

[6] Kang, D.; Kwon, J. Y.; Cho, H.; Sim, J.-H.; Hwang, H. S.; Kim, C. S.; Kim, Y. J.; Ruoff, R. S.; Shin, H. S. Oxidation Resistance of Iron and Copper Foils Coated with Reduced Graphene Oxide Multilayers. ACS Nano 2012, 6 (9), 7763–7769. (1) https://doi.org/10.1021/nn3017316.

[7] Prasai, D.; Tuberquia, J. C.; Harl, R. R.; Jennings, G. K.; Rogers, B. R.; Bolotin, K. I. Graphene: Corrosion-Inhibiting Coating. ACS Nano 2012, 6 (2), 1102–1108. https://doi.org/10.1021/nn203507y.

[8] Bunch, J. S.; van der Zande, A. M.; Verbridge, S. S.; Frank, I. W.; Tanenbaum, D. M.; Parpia, J. M.; Craighead, H. G.; McEuen, P. L. Electromechanical Resonators from Graphene Sheets. Science 2007, 315 (5811), 490–493. https://doi.org/10.1126/science.1136836.

[9] Schriver, M.; Regan, W.; Gannett, W. J.; Zaniewski, A. M.; Crommie, M. F.; Zettl, A. Graphene as a Long-Term Metal Oxidation Barrier: Worse than Nothing. ACS Nano 2013, 7 (7), 5763–5768. https://doi.org/10.1021/nn4014356.

[10] Mahvash, F.; Eissa, S.; Bordjiba, T.; Tavares, A. C.; Szkopek, T.; Siaj, M. Corrosion Resistance of Monolayer Hexagonal Boron Nitride on Copper. Scientific Reports 2017, 7 (1), 42139. https://doi.org/10.1038/srep42139.

[11] Li, L. H.; Xing, T.; Chen, Y.; Jones, R. Boron Nitride Nanosheets for Metal Protection. Advanced Materials Interfaces 2014, 1 (8), 1300132. https://doi.org/10.1002/admi.201300132.

[12] Yi, M.; Shen, Z.; Zhao, X.; Liang, S.; Liu, L. Boron Nitride Nanosheets as Oxygen-Atom Corrosion Protective Coatings. Appl. Phys. Lett. 2014, 104 (14), 143101. https://doi.org/10.1063/1.4870530.

[13]Kim, E.; Jain, N.; Jacobs-Gedrim, R.; Xu, Y.; Yu, B. Exploring Carrier Transport Phenomena in a CVD-Assembled Graphene FET on Hexagonal Boron Nitride. Nanotechnology 2012, 23 (12), 125706. https://doi.org/10.1088/0957-4484/23/12/125706.

[14] Gibb, A. L.; Alem, N.; Chen, J.-H.; Erickson, K. J.; Ciston, J.; Gautam, A.; Linck, M.; Zettl, A. Atomic Resolution Imaging of Grain Boundary Defects in Monolayer Chemical Vapor Deposition-Grown Hexagonal Boron Nitride. J. Am. Chem. Soc. 2013, 135 (18), 6758–6761. https://doi.org/10.1021/ja400637n.

[15] Pakdel, A.; Zhi, C.; Bando, Y.; Nakayama, T.; Golberg, D. Boron Nitride Nanosheet Coatings with Controllable Water Repellency. ACS Nano 2011, 5 (8), 6507–6515. https://doi.org/10.1021/nn201838w.

[16] Tamura, M.; Noma, M.; Yamashita, M. Characteristic Change of Hydrogen Permeation in Stainless Steel Plate by BN Coating. Surface and Coatings Technology 2014, 260, 148–154. https://doi.org/10.1016/j.surfcoat.2014.09.041.

[17] Li, G.-X.; Liu, Y.; Wang, B.; Song, X.-M.; Li, E.; Yan, H. Preparation of Transparent BN Films with Superhydrophobic Surface. Applied Surface Science 2008, 254 (17), 5299–5303. https://doi.org/10.1016/j.apsusc.2008.01.170
[18] Warner, J. H.; Rümmeli, M. H.; Bachmatiuk, A.; Büchner, B. Atomic Resolution Imaging and Topography of Boron Nitride Sheets Produced by Chemical Exfoliation. ACS Nano 2010, 4 (3), 1299–1304. https://doi.org/10.1021/nn901648q.
[19] Li, X.; Hao, X.; Zhao, M.; Wu, Y.; Yang, J.; Tian, Y.; Qian, G. Exfoliation of Hexagonal Boron Nitride by Molten Hydroxides. Advanced Materials 2013, 25 (15), 2200–2204. https://doi.org/10.1002/adma.201204031.
[20] TabkhPaz, M.; Park, D.-Y.; Lee, P. C.; Hugo, R.; Park, S. S. Development of Nanocomposite Coatings with Improved Mechanical, Thermal, and Corrosion Protection Properties. Journal of Composite Materials 2018, 52 (8), 1045–1060. https://doi.org/10.1177/0021998317720001.
[21] Huang, Y.-C.; Lo, T.-Y.; Chao, C.-G.; Whang, W.-T. Anti-Corrosion Characteristics of Polyimide/h-Boron Nitride Composite Films with Different Polymer Configurations. Surface and Coatings Technology 2014, 260, 113–117. https://doi.org/10.1016/j.surfcoat.2014.09.043.
[22] Husain, E.; Narayanan, T. N.; Taha-Tijerina, J. J.; Vinod, S.; Vajtai, R.; Ajayan, P. M. Marine Corrosion Protective Coatings of Hexagonal Boron Nitride Thin Films on Stainless Steel. ACS Appl Mater Interfaces 2013, 5 (10), 4129–4135. https://doi.org/10.1021/am400016y.
[23] Coan, T.; Barroso, G. S.; Motz, G.; Bolzán, A.; Machado, R. a. F. Preparation of PMMA/HBN Composite Coatings for Metal Surface Protection. Materials Research 2013, 16 (6), 1366–1372. https://doi.org/10.1590/S1516-14392013005000140.
[24] Mj, C.; Sm, R.; J, C.; S, L.; Gg, Z.; Hc, Z.; Lp, W.; Qj, X. Anticorrosive performance of waterborne epoxy coatings containing water-dispersible hexagonal boron nitride (h-BN) nanosheets. Appl. Surf. Sci. 2017, 397, 77–86.
[25] Golberg, D.; Bando, Y.; Huang, Y.; Terao, T.; Mitome, M.; Tang, C.; Zhi, C. Boron Nitride Nanotubes and Nanosheets. ACS Nano 2010, 4 (6), 2979–2993. https://doi.org/10.1021/nn1006495.
[26] Kim, K.; Kim, M.; Hwang, Y.; Kim, J. Chemically Modified Boron Nitride-Epoxy Terminated Dimethylsiloxane Composite for Improving the Thermal Conductivity. Ceram. Int. 2014, 40 (1 PART B), 2047–2056. https://doi.org/10.1016/j.ceramint.2013.07.117. https://doi.org/10.1016/j.ceramint.2013.07.117.
[27] Yu, J.; Zhao, W.; Liu, G.; Wu, Y.; Wang, D. Anti-Corrosion Mechanism of 2D Nanosheet Materials in Waterborne Epoxy Coatings. Surface Topography: Metrology and Properties 2018, 6, 034019. https://doi.org/10.1088/2051-672X/aad5ab.
[28] Fan, Y.; Yang, H.; Fan, H.; Liu, Q.; Lv, C.; Zhao, X.; Yang, M.; Wu, J.; Cao, X. Corrosion Resistance of Modified Hexagonal Boron Nitride (h-BN) Nanosheets Doped Acrylic Acid Coating on Hot-Dip Galvanized Steel. Materials (Basel) 2020, 13 (10). https://doi.org/10.3390/ma13102340.
[29] Ysiwata-Rivera, A. P.; Hernández-Hernández, E.; Cadenas-Pliego, G.; Ávila-Orta, C. A.; González-Morones, P.; Jesús, J. A. V.; Cuara-Díaz, E.; Gallardo-Vega, C. A.; Mata-Padilla, J. M. Effect of Modified Hexagonal Boron Nitride Nanoparticles on the Emulsion Stability, Viscosity and Electrochemical Behavior of Nanostructured Acrylic Coatings for the Corrosion Protection of AISI 304 Stainless Steel. Coatings 2020, 10 (5), 488. https://doi.org/10.3390/coatings10050488.
[30] Martin, P. M., Ed.; Chapter 3 - Surface Preparation for Film and Coating Deposition Processes. In Handbook of Deposition Technologies for Films and Coatings (Third Edition); William Andrew Publishing: Boston, 2010; pp 93–134.
[31] Nouri, E.; Shahmiri, M.; Rezaie, H. R.; Talayian, F. A Comparative Study of Heat Treatment Temperature Influence on the Thickness of Zirconia Sol–Gel Thin Films by Three Different Techniques: SWE, SEM and AFM. Surface and Coatings Technology 2012, 206 (19–20), 3809–3815. https://doi.org/10.1016/j.surfcoat.2011.11.030
[32] Jorcin, J.-B.; Orazem, M. E.; Pébère, N.; Tribollet, B. CPE Analysis by Local Electrochemical Impedance Spectroscopy. Electrochimica Acta 2006, 51 (8–9), 1473–1479. https://doi.org/10.1016/j.electacta.2005.02.128.

[33] Lin, Y.; Williams, T. V.; Xu, T.-B.; Cao, W.; Elsayed-Ali, H. E.; Connell, J. W. Aqueous Dispersions of Few-Layered and Monolayered Hexagonal Boron Nitride Nanosheets from Sonication-Assisted Hydrolysis: Critical Role of Water. J. Phys. Chem. C 2011, 115 (6), 2679–2685. https://doi.org/10.1021/jp110985w.

[34] O'Brien, S. A.; Harvey, A.; Griffin, A.; Donnelly, T.; Mulcahy, D.; Coleman, J. N.; Donegan, J. F.; McCloskey, D. Light Scattering and Random Lasing in Aqueous Suspensions of Hexagonal Boron Nitride Nanoflakes. Nanotechnology 2017, 28 (47), 47LT02. https://doi.org/10.1088/1361-6528/aa923a.

[35] Brug, G.; Vandeneeden, A.; Sluytersrehbach, M.; Sluyters, J. The Analysis of Electrode Impedances Complicated by the Presence of a Constant Phase Element. J. Electroanal. Chem. 1984, 176 (1–2), 275–295.

[36] Coleman, J. N.; Lotya, M.; O'Neill, A.; Bergin, S. D.; King, P. J.; Khan, U.; Young, K.; Grieveson, E. M.; Theuwissen, K.; McComb, D. W.; Nellist, P. D.; Nicolosi, V. Two-Dimensional Nanosheets Produced by Liquid Exfoliation of Layered Materials. Science 2011, 331 (6017), 568–571. https://doi.org/10.1126/science.1194975.

[37] Kim, J.; Kwon, S.; Cho, D.-H.; Kang, B.; Kwon, H Byun, D.; Lee, Z.; Lee, C. Direct Exfoliation and Dispersion of Two-Dimensional Materials in Pure Water via Temperature Control. Nat Commun 2015, 6, 8294. https://doi.org/10.1038/ncomms9294.

[38] Feng, P.; Chavez, E.; Malca, C. Super Stable Pollution Gas Sensor Based on Functionalized 2D Boron Nitride Nanosheet Materials for High Humidity Environments. Chemosensors 2018, 6 (4), 49. https://doi.org/10.3390/chemosensors6040049

[39] Metroke, T. L.; Kachurina, O.; Knobbe, E. T. Spectroscopic and Corrosion Resistance Characterization of GLYMO–TEOS Ormosil Coatings for Aluminum Alloy Corrosion Inhibition. Progress in Organic Coatings 2002, 44 (4), 295–305. https://doi.org/10.1016/S0300-9440(02)00063-2

[40] Tackett, J. E. FT-IR Characterization of Metal Acetates in Aqueous Solution: Applied Spectroscopy 2016. https://doi.org/10.1366/0003702894202931.

[41] Densification and Aging of ZrO2 Films Prepared by Sol–Gel. Thin Solid Films 2001, 392 (1), 142–148. https://doi.org/10.1016/S0040-6090(01)01009-4.

[42] Luo, X.; Zhang, Y.; Zandén, C.; Murugesan, M.; Cao, Y.; Ye, L.; Liu, J. Novel Thermal Interface Materials: Boron Nitride Nanofiber and Indium Composites for Electronics Heat Dissipation Applications. J Mater Sci: Mater Electron 2014, 25 (5), 2333–2338. https://doi.org/10.1007/s10854-014-1880-8.

[43] SigmaAldrich. IR Spectrum Table & Chart. https://www.sigmaaldrich.com/technical-documents/articles/biology/ir-spectrum-table.html

[44] Selvam, N. C. S.; Manikandan, A.; Kennedy, L. J.; Vijaya, J. J. Comparative Investigation of Zirconium Oxide (ZrO2) Nano and Microstructures for Structural, Optical and Photocatalytic Properties. Journal of Colloid and Interface Science 2013, 389 (1), 91–98. https://doi.org/10.1016/j.jcis.2012.09.014.

[45] Chen, S.; Yin, Y.; Wang, D.; Liu, Y.; Wang, X. Structures, Growth Modes and Spectroscopic Properties of Small Zirconia Clusters. Journal of Crystal Growth 2005, 282 (3), 498–505. https://doi.org/10.1016/j.jcrysgro.2005.05.017.

[46] Nemanich, R. J.; Solin, S. A.; Martin, R. M. Light Scattering Study of Boron Nitride Microcrystals. Phys. Rev. B 1981, 23 (12), 6348–6356. https://doi.org/10.1103/PhysRevB.23.6348.

[47] Perry, C. H.; Liu, D.-W.; Ingel, R. P. Phase Characterization of Partially Stabilized Zirconia by Raman Spectroscopy. Journal of the American Ceramic Society 1985, 68 (8), C-184-C–187. https://doi.org/10.1111/j.1151-2916.1985.tb10176.x.

[48] Zhang, M.; Salje, E. K. H.; Farnan, I.; Graeme-Barber, A.; Daniel, P.; Ewing, R. C.; Clark, A. M.; Leroux, H. Metamictization of Zircon: Raman Spectroscopic Study. J. Phys.: Condens. Matter 2000, 12 (8), 1915–1925.

[49] Craig, B. D. Thermodynamics of Corrosion. In Fundamental Aspects of Corrosion Films in Corrosion Science; Craig, B. D., Ed.; Springer US: Boston, MA, 1991

[50] Goetz, R.; Landolt, D. The Influence of Chromium Content and Potential on the Surface Composition of Fe-Cr-Mo Alloys Studied by AES. Electrochimica Acta 1984, 29 (5), 667–676. https://doi.org/10.1016/0013-4686(84)87126-1.
[51] Zuo, Y.; Wang, H.; Zhao, J.; Xiong, J. The Effects of Some Anions on Metastable Pitting of 316L Stainless Steel. Corrosion Science 2002, 44 (1), 13–24.
[52] Boissy, Clémont (2014). Doctoral dissertation: Transport de matière au sein du film passif : Développement d'une méthodologie sélective corrélant les Point Defect Model et les modèles descriptifs. INSA de Lyon, Villeurbanne, France.
[53] Boissy, C.; Ter-Ovanessian, B.; Mary, N.; Normand, B. Correlation between Predictive and Descriptive Models to Characterize the Passive Film – Study of Pure Chromium by Electrochemical Impedance Spectroscopy. Electrochimica Acta 2015, 174, 430–437. https://doi.org/10.1016/j.electacta.2015.05.179.
[54] Ćurković, L.; Ćurković, H. O.; Salopek, S.; Renjo, M. M.; Šegota, S. Enhancement of Corrosion Protection of AISI 304 Stainless Steel by Nanostructured Sol–Gel TiO2 Films. Corrosion Science 2013, 77, 176–184. https://doi.org/10.1016/j.corsci.2013.07.045.
[55] Hirschorn, B.; Orazem, M. E.; Tribollet, B.; Vivier, V.; Frateur, I.; Musiani, M. Determination of Effective Capacitance and Film Thickness from Constant-Phase-Element Parameters. Electrochimica Acta 2010, 55 (21), 6218–6227. https://doi.org/10.1016/j.electacta.2009.10.065.

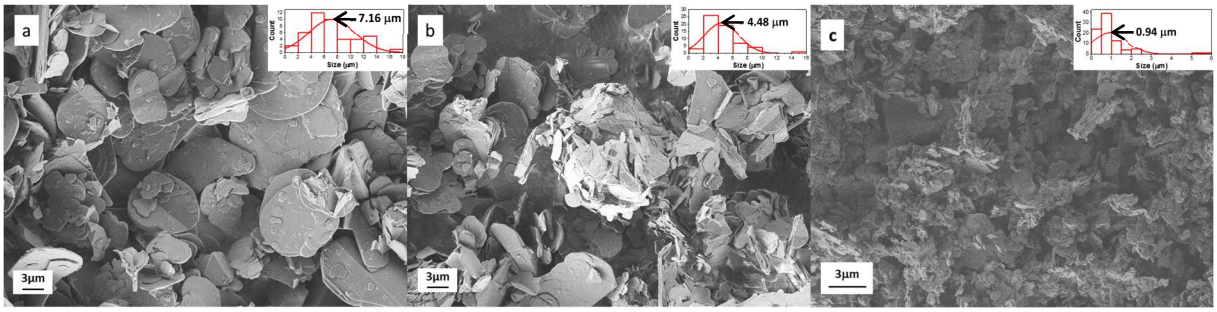

Fig.1 the morphology of raw materials of a) BN-A, b) BN-B and c) BN-C

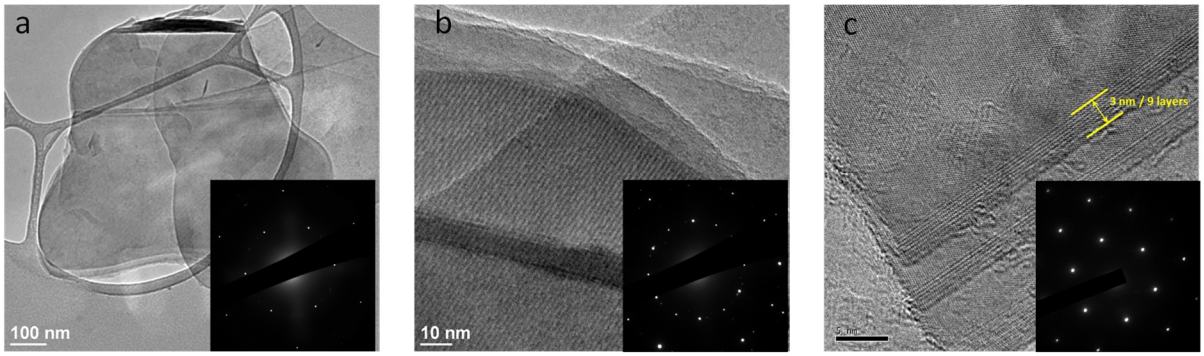

Fig. 2 the TEM image for different exfoliation states: a) single crystal, b) misorientation induced by the exfoliation treatment and c) few-layered BNNS. The inset is the corresponding selective area electron diffraction.

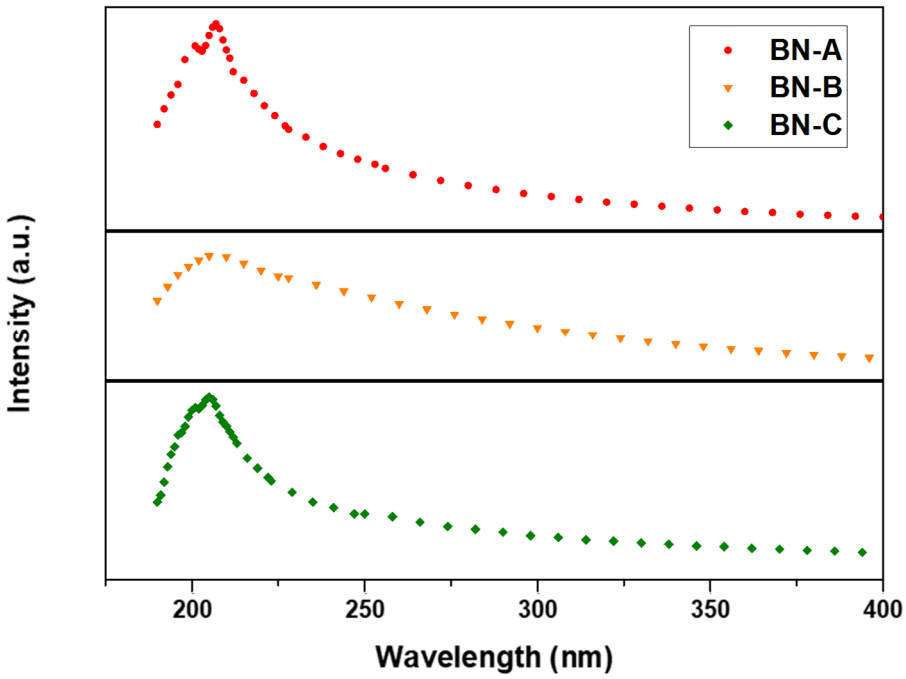

Fig.3 the UV-Visible Spectroscopy obtained with BNNS colloidal solution issued from the different raw h-BN powders

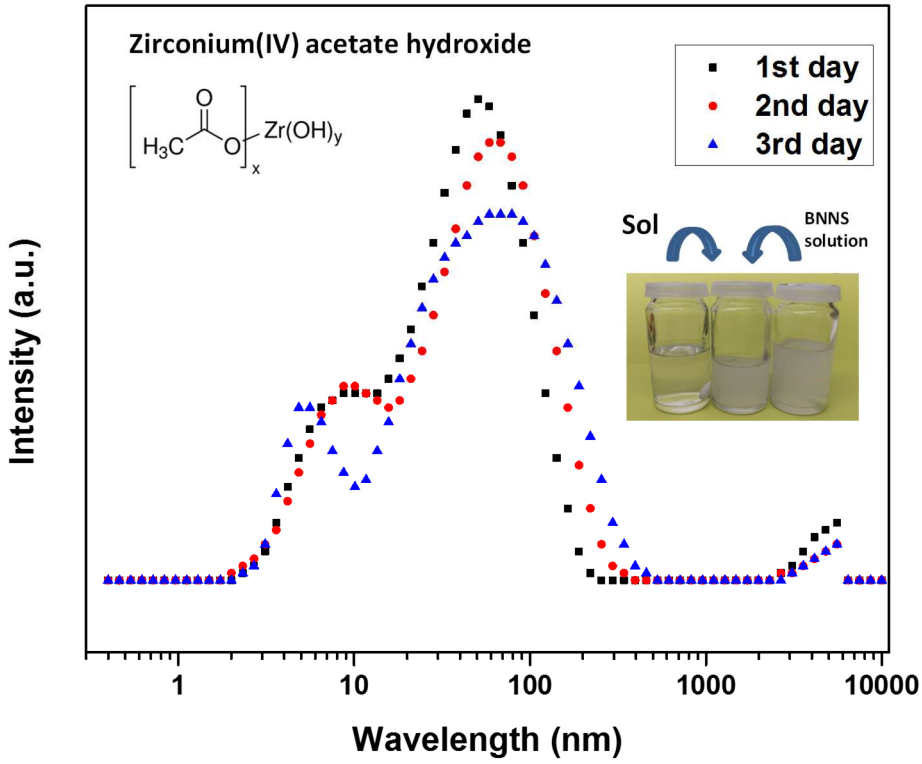

Fig. 4 The DLS curves of ZrO solution without charge in three days

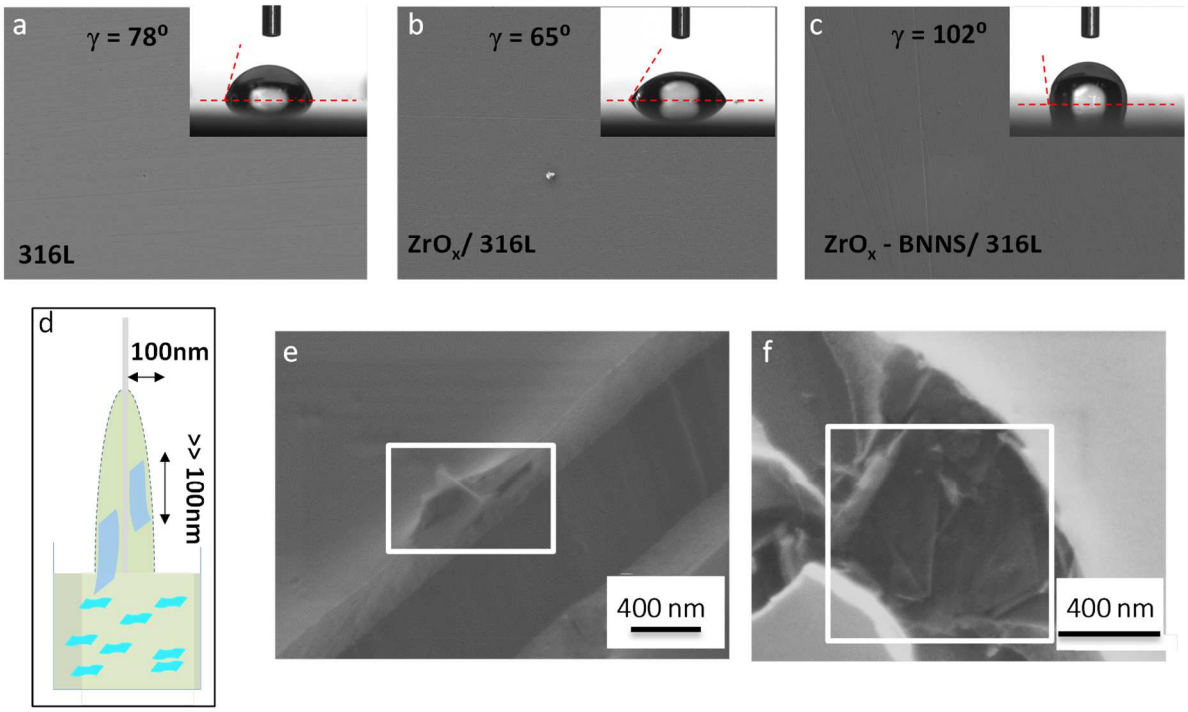

Fig. 5 SEM images of the surface of a) 316L surface, b) ZrO and c) ZrO/BN coating. The statistic water contact angles on different surfaces are shown inset. d) the scheme of dip-coating and the orientation of BNNS, e) and f)the SEM images of the existence of BNNS in the matrix.

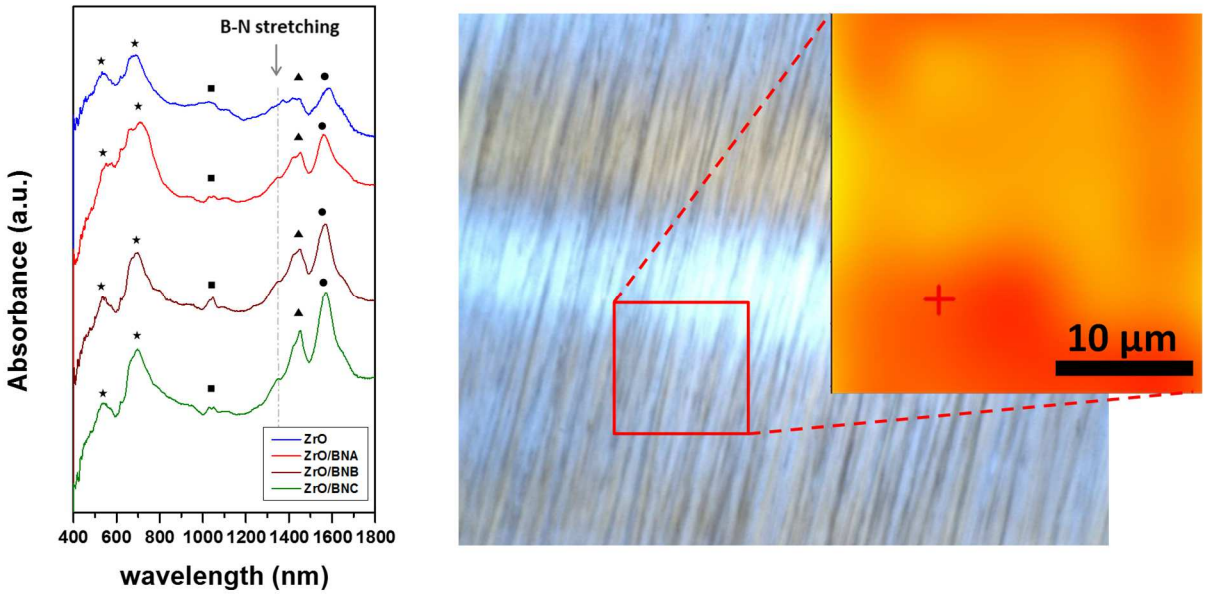

Fig. 6: FTIR spectra of ZrO and the three nanocomposite ZrO/BN coating on the left side. (Arrow for B-N stretching; the ▲and ● are attribuated to -CO_2 groups of the sol-gel matrix; ■ reprensts the C-O stretching; ★corresponds to the Zr-O-Zr in the matrix); On the right side, the intensity mapping of B-N stretch band, where the color intensity represents the relative quantity of B-N banding.

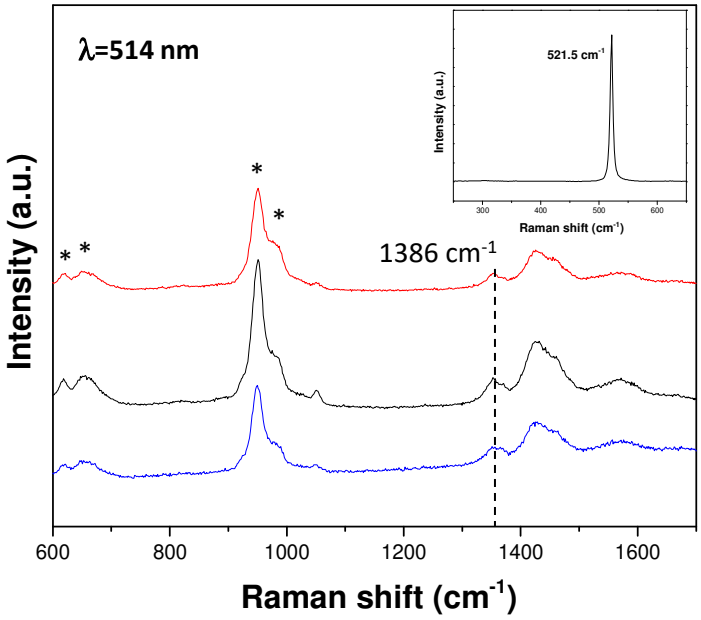

Fig. 7: Typical Raman spectra obtained with randomly selected points on ZrO/BN coatings. The inset shows the calibration with silicon.

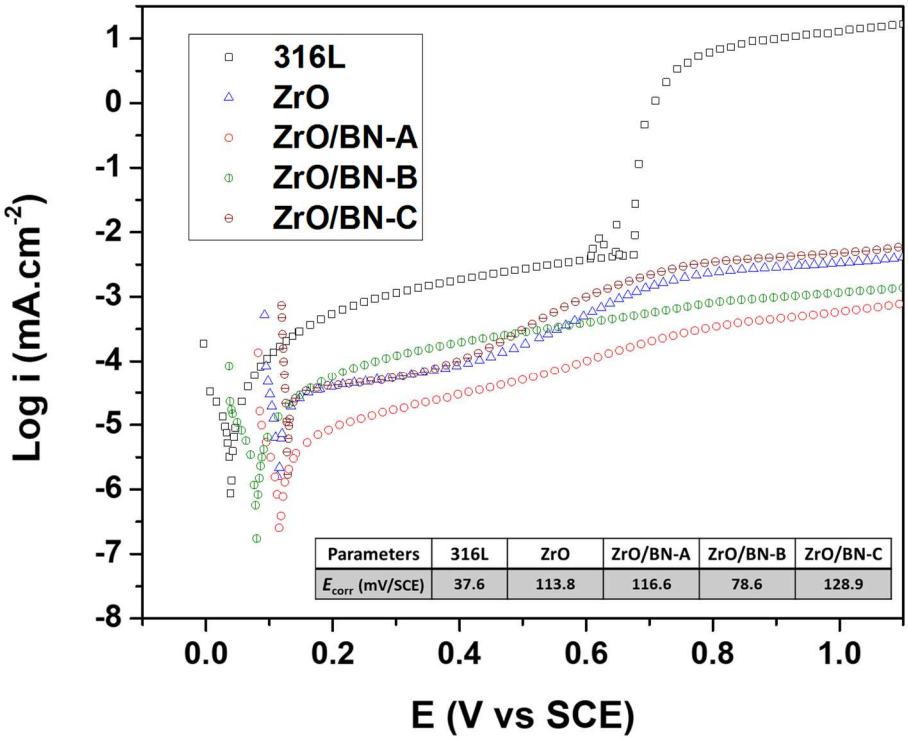

Fig.8: Electrochemical dynamic polarization curves in NaCl 30g/L of 316L, ZrO and charged samples. Inset the table of corrosion potential E_{corr} of different samples

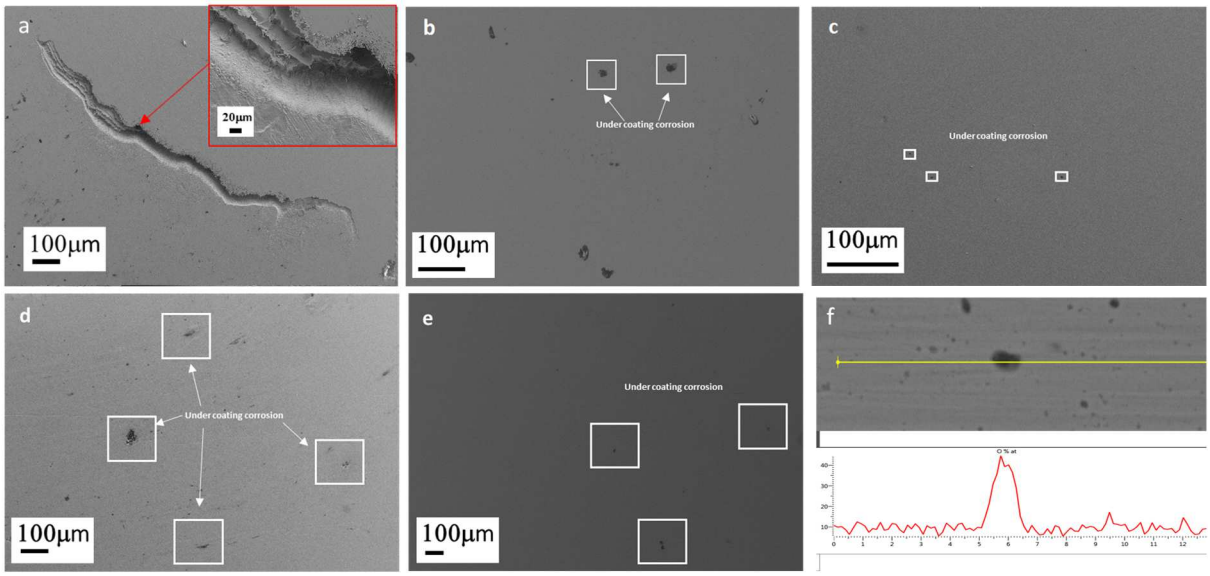

Fig.9: SEM image of the surface morphology obtained with a) 316L, b) ZrO, c) ZrO/BN-A, d) ZrO/BN-B, e) ZrO/BN-C, and f) SEM image around an oxidation site and the chemical analysis by energy dispersive spectroscopy (EDS)

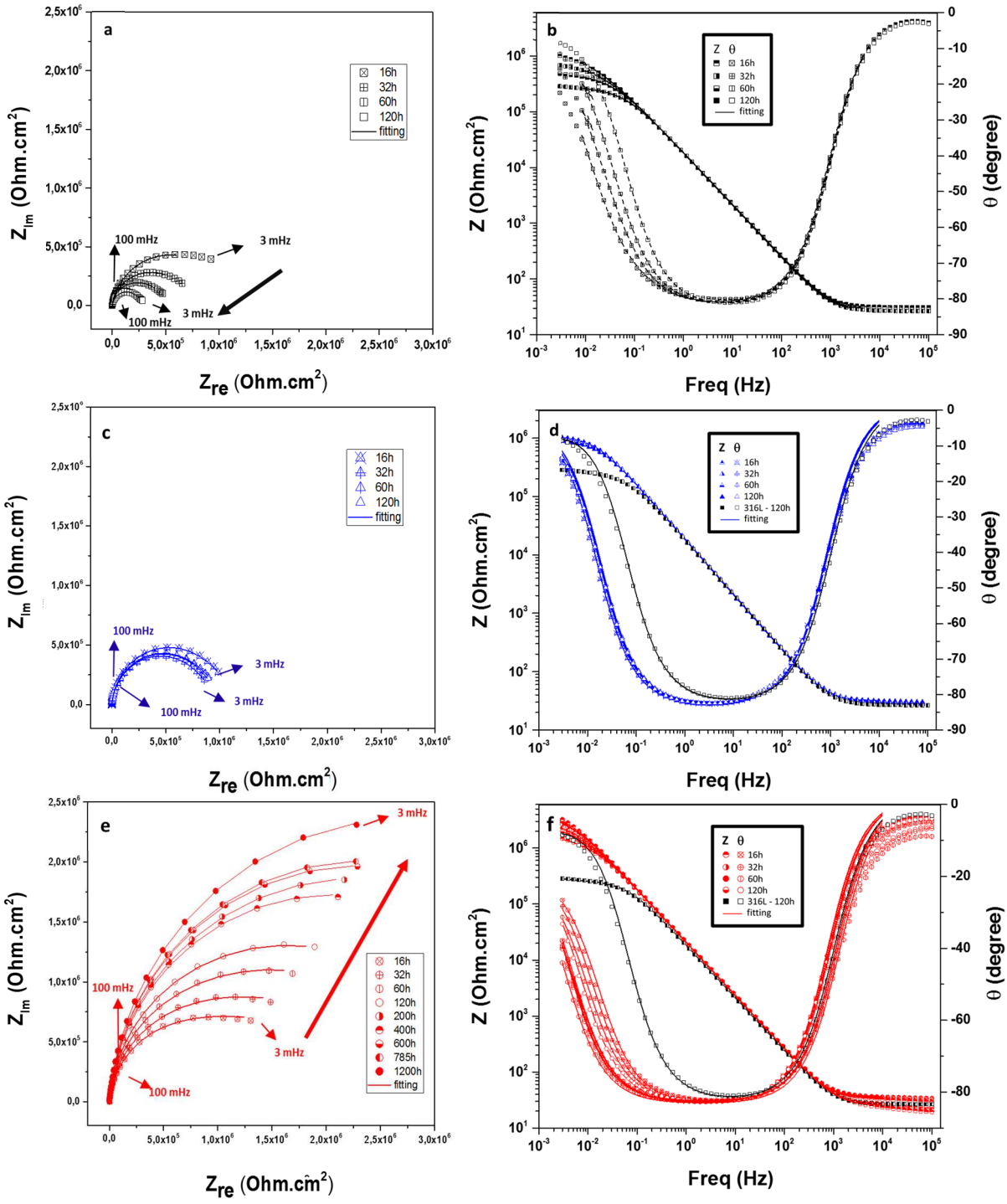

Fig. 10: Nyquist and Bode curve obtained with a) and b) 316L, c) and d) ZrO, e) and f) ZrO/BN-A

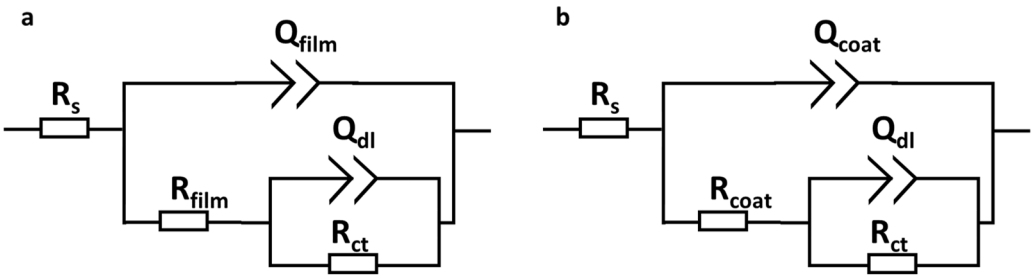

Fig. 11 equivalent circuit for a) 316L and b) ZrO and ZrO/BN-A

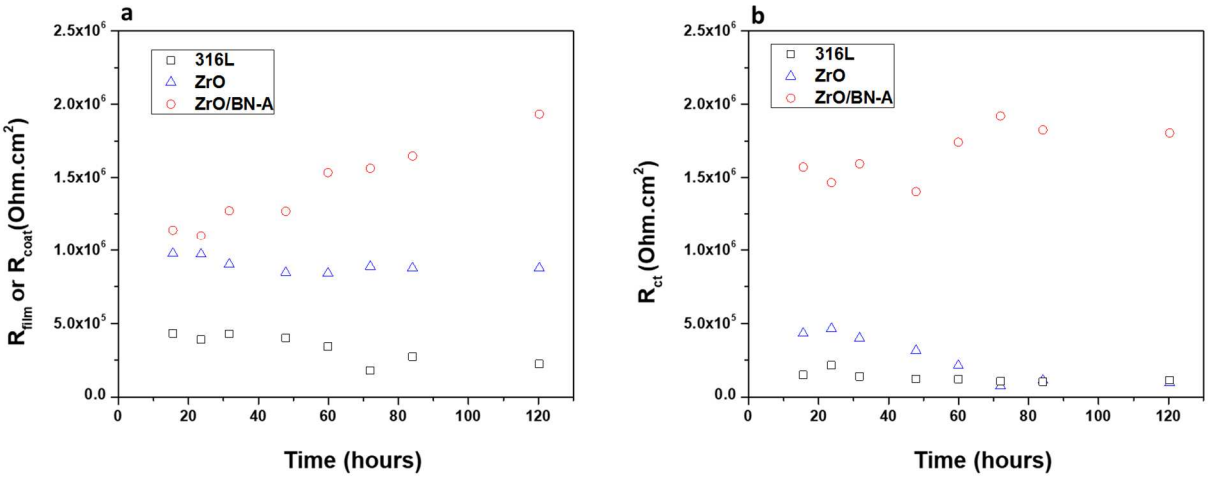

Fig. 12: The variation of EIS fitting parameter value a) R_{film} or R_{coat}, b) R_{ct} over 120 hours of the three samples

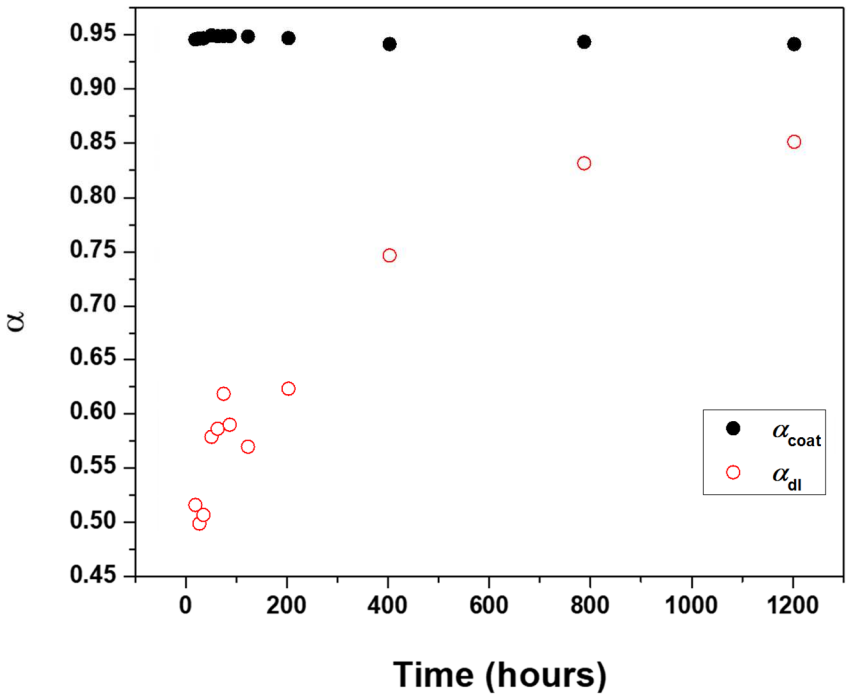

Fig. 13 The variation of α values over 1200h obtained with ZrO/BN-A

Table 1: The fitting parameters of EIS for bare 316L, ZrO, and ZrO/BN-A after 16 and 120h of immersion. For ZrO/BN-A the parameter obtained after 1200h of immersion are presented as well.

Uncoated Sample	R_s **(ohm.cm^2)**	R_{film} **(x10^5 ohm.cm^2)**	α_{film}	Q_{film} **(x10^{-6} f.s^(α-1))**	R_{ct} **(x10^5 ohm.cm^2)**	α_{dl}	Q_{dl} **(x10^{-6} f.s^(α-1))**
316L 16h	30.8 ± 0.2	4.33 ± 5.40x10^{-4}	0.93 ±0.01	9.67 ± 1.10 x10^{-3}	4.32 ± 2.40x10^{-3}	0.56 ± 0.01	3.59 ± 7.00 x10^{-3}
316L 120h	26.6 ± 0.2	2.26 ± 3.35 x10^{-3}	0.94 ±0.01	9.54 ± 3.60 x10^{-3}	0.99 ± 1.73x10^{-3}	0.50 ± 0.01	4.75 ± 6.40 x10^{-3}
Coated Sample	R_s **(ohm.cm^2)**	R_{coat} **(x10^5 ohm.cm^2)**	α_{coat}	Q_{coat} **(f.s^(α-1))**	R_{ct} **(ohm.cm^2)**	α_{dl}	Q_{dl} **(f.s^(α-1))**
ZrO 16h	32.9 ± 0.2	9.73 ± 2.20 x10^{-4}	0.95± 0.01	9.32 ± 8.71 x10^{-6}	1.53 ± 1.37x10^{-3}	0.73 ± 0.01	6.11 ± 0.30 x10^{-6}
ZrO 120h	36.8 ± 0.2	8.74 ± 1.80 x10^{-4}	0.95± 0.01	9.22 ± 9.07 x10^{-6}	1.16 ± 1.51x10^{-3}	0.73 ± 0.01	7.85 ± 2.80 x10^{-6}
ZrO/BN-A 16h	35.6 ± 0.2	11.41 ± 3.50 x10^{-4}	0.95± 0.01	8.76 ± 6.40 x10^{-6}	15.61 ± 1.42x10^{-3}	0.52 ± 0.01	9.33 ± 2.10 x10^{-6}
ZrO/BN-A 120h	35.3 ± 0.2	19.22 ± 8.00 x10^{-4}	0.95± 0.01	8.66 ± 8.41 x10^{-6}	16.12 ± 1.19x10^{-3}	0.57 ± 0.01	4.72 ± 1.60 x10^{-6}
ZrO/BN-A 1200h	24.6 ± 0.2	47.35 ± 1.10 x10^{-3}	0.94± 0.01	8.53 ± 8.71 x10^{-6}	17.81 ± 2.84x10^{-3}	0.85 ± 0.01	4.41 ± 1.30 x10^{-6}

Graphical Abstract